

The contribution of radio-frequency rectification to field-aligned losses of high-harmonic fast wave power to the divertor in the National Spherical Torus eXperiment

R. J. Perkins, J. C. Hosea, M. A. Jaworski, J.-W. Ahn, A. Diallo, R. E. Bell, N. Bertelli, S. Gerhardt, T. K. Gray, G. J. Kramer, B. P. LeBlanc, A. McLean, C. K. Phillips, M. Podestà, L. Roquemore, S. Sabbagh, G. Taylor, and J. R. Wilson

Citation: *Physics of Plasmas* **22**, 042506 (2015); doi: 10.1063/1.4916034

View online: <http://dx.doi.org/10.1063/1.4916034>

View Table of Contents: <http://scitation.aip.org/content/aip/journal/pop/22/4?ver=pdfcov>

Published by the **AIP Publishing**

Articles you may be interested in

[Numerical investigation of fast-wave propagation and radio-frequency sheath interaction with a shaped tokamak wall](#)

Phys. Plasmas **22**, 072504 (2015); 10.1063/1.4926449

[Radio-frequency sheaths physics: Experimental characterization on Tore Supra and related self-consistent modeling](#)

Phys. Plasmas **21**, 061509 (2014); 10.1063/1.4884778

[Advances in high-harmonic fast wave physics in the National Spherical Torus Experimenta\)](#)

Phys. Plasmas **17**, 056114 (2010); 10.1063/1.3371956

[Parametric study of two-dimensional potential structures induced by radio-frequency sheaths coupled with transverse currents in front of the Ion Cyclotron Resonance Heating antenna](#)

Phys. Plasmas **13**, 042512 (2006); 10.1063/1.2186530

[Edge ion heating by launched high harmonic fast waves in the National Spherical Torus Experimenta\)](#)

Phys. Plasmas **12**, 056108 (2005); 10.1063/1.1871953



PFEIFFER VACUUM

VACUUM SOLUTIONS FROM A SINGLE SOURCE

Pfeiffer Vacuum stands for innovative and custom vacuum solutions worldwide, technological perfection, competent advice and reliable service.

125 YEARS NOTHING IS BETTER

The contribution of radio-frequency rectification to field-aligned losses of high-harmonic fast wave power to the divertor in the National Spherical Torus eXperiment

R. J. Perkins,^{1(a)} J. C. Hosea,¹ M. A. Jaworski,¹ J.-W. Ahn,² A. Diallo,¹ R. E. Bell,¹ N. Bertelli,¹ S. Gerhardt,¹ T. K. Gray,² G. J. Kramer,¹ B. P. LeBlanc,¹ A. McLean,³ C. K. Phillips,¹ M. Podestà,¹ L. Roquemore,¹ S. Sabbagh,⁴ G. Taylor,¹ and J. R. Wilson¹

¹Princeton Plasma Physics Laboratory, Princeton, New Jersey 08543, USA

²Oak Ridge National Laboratory, Oak Ridge, Tennessee 37831, USA

³Lawrence Livermore National Laboratory, Livermore, California 94550, USA

⁴Department of Applied Physics and Applied Mathematics, Columbia University, New York, New York 10027, USA

(Received 24 December 2014; accepted 27 February 2015; published online 13 April 2015)

The National Spherical Torus eXperiment (NSTX) can exhibit a major loss of high-harmonic fast wave (HHFW) power along scrape-off layer (SOL) field lines passing in front of the antenna, resulting in bright and hot spirals on both the upper and lower divertor regions. One possible mechanism for this loss is RF sheaths forming at the divertors. Here, we demonstrate that swept-voltage Langmuir probe characteristics for probes under the spiral are shifted relative to those not under the spiral in a manner consistent with RF rectification. We estimate both the magnitude of the RF voltage across the sheath and the sheath heat flux transmission coefficient in the presence of the RF field. Although precise comparison between the computed heat flux and infrared (IR) thermography cannot yet be made, the computed heat deposition compares favorably with the projections from IR camera measurements. The RF sheath losses are significant and contribute substantially to the total SOL losses of HHFW power to the divertor for the cases studied. This work will guide future experimentation on NSTX-U, where a wide-angle IR camera and a dedicated set of coaxial Langmuir probes for measuring the RF sheath voltage directly will quantify the contribution of RF sheath rectification to the heat deposition from the SOL to the divertor. © 2015 AIP Publishing LLC. [<http://dx.doi.org/10.1063/1.4916034>]

I. INTRODUCTION

Plasma heating using waves in the ion-cyclotron range of frequencies (ICRF) is an important auxiliary heating technique for tokamaks, and up to 20 MW of ICRF power is planned for ITER.¹ With respect to the spherical-tokamak geometry, high-harmonic fast-wave heating (HHFW)² is envisioned to aid in plasma start-up to help obtain completely non-inductive operation.³ There are several issues in both scrape off layer (SOL) and core-plasma physics for which it is important to know how much fast-wave power is coupled to the core plasma and how much is lost to the SOL; these physics issues include modeling plasma start-up, fast-wave absorption by fast ions,^{4–6} and the RF losses to the divertor plates via the SOL.

One outstanding issue regarding HHFW heating experiments on the National Spherical Torus eXperiment (NSTX)⁷ is a significant power loss that can occur directly in the SOL,⁸ producing bright and hot spirals on both the upper and lower divertor regions,^{9–11} as shown in Fig. 1. For shot 130 621, only approximately 40% of the RF power coupled from the antenna reaches the core plasma, while an infrared (IR) camera¹² measures an RF-produced heat flux within the spiral of up to ~ 2 MW/m² (Ref. 9) ($k_\phi = -8$ m⁻¹ or -90° phasing between antenna straps, and $P_{RF} = 1.8$ MW/m²), although the peak

observed heat flux is typically smaller. The heating efficiency of the HHFW system is a strong function of the magnetic field strength, the toroidal wavenumber k_ϕ , and the edge density,^{8–11} suggesting that the SOL losses are intimately connected with the location of the righthand cutoff, a hypothesis that is being observed in full-wave simulations.¹³ Importantly, these spirals have been shown to be the footprints of SOL field lines that pass directly in front of the antenna,¹⁴ as has been determined by field-line mapping using the SPIRAL code,¹⁵ as shown in Fig. 2(a) for shot 141 899. This includes all SOL field lines passing in front of the antenna between the antenna and the last closed flux surface (LCFS), and not just those lines connected to antenna components. Other diagnostics for investigating the RF heat deposition on the divertor include both a four-element radial array of swept-voltage Langmuir probes in the lower divertor region,^{16,17} and divertor tiles that have been instrumented to measure currents.¹⁸ The locations of these diagnostics relative to the RF spiral are shown in Figs. 1 and 2(b).

This paper demonstrates, for selected discharges with both RF and neutral beam (NB) power and with only RF power, that RF rectified sheaths are playing an important role in this SOL loss of fast-wave power to the divertor. RF rectification, reviewed in Sec. III, occurs when an oscillating RF electric field develops across the sheath at the wall or probe, and results in an enhanced DC electron current at a given bias voltage.^{19,20} RF rectification is often studied in

^{a)}E-mail: rperkins@pppl.gov

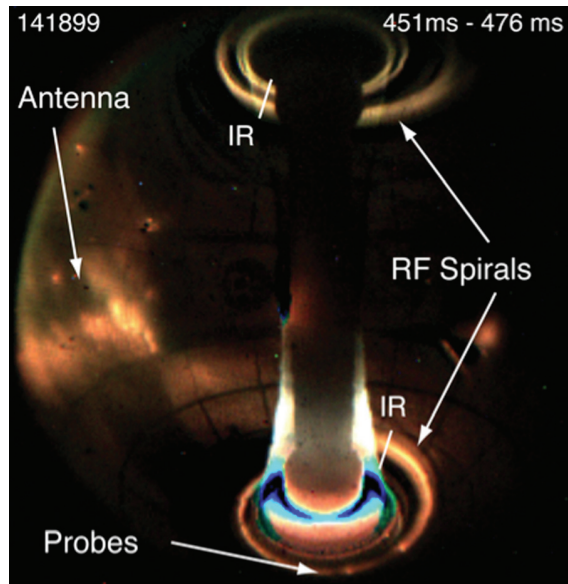


FIG. 1. RF spirals produced on the bottom and top divertor plates of NSTX with HHFW heating. IR measurement locations are at Bay I bottom and Bay G top as indicated. Four swept-voltage Langmuir probes are located at Bay B just outboard of the vessel gap. Plasma conditions are $B_T = 4.5$ kG, $I_p = 1.0$ MA (magnetic pitch in the SOL $\sim 39.6^\circ$), $P_{RF} = 1.3$ MW, $P_{NB} = 2$ MW, and deuterium.

the vicinity of the antenna structure as a possible explanation for impurity injection during ICRF operation^{21–23} and to explain RF-induced heat fluxes and hot spots on the antenna structure.^{24,25} In this work, we consider specifically the

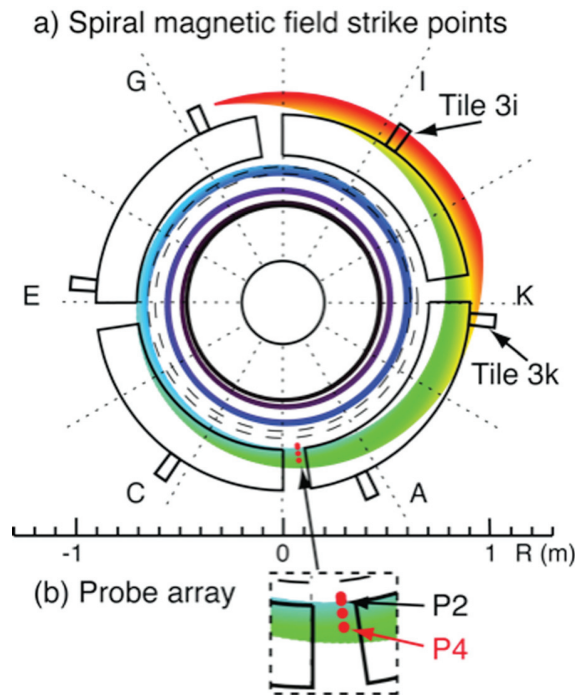


FIG. 2. (a) Calculated spiral location on the bottom divertor using the SPIRAL code for field lines passing in front of the HHFW antenna in the SOL. Color signifies the radial location of the field line at the midplane: red is near the antenna and black is near the LCFS. Conditions of Fig. 1, shot 141 899 at 433 ms. (b) Expanded view of four probes at Bay B. Probe R (cm) values 1–4: 63.82, 64.67, 67.49, and 70.59.

effect of RF rectification on producing the RF heat deposition on the divertor plates in NSTX, a case that is sometimes referred to as a far-field sheath.²⁶ Far-field RF sheaths have been cited as a source of multi-pass damping for regimes where the wave energy is poorly absorbed in the core plasma and circulates through the torus, with a small percentage of the RF power being lost through interactions with the wall via the sheath.²⁷ Because NSTX produces high-beta plasma with strong single pass absorption in the HHFW regime, the RF spirals and associated losses are direct effects and occur for waves propagating through the SOL away from the antenna but before they cross the last closed flux surface.^{8,10}

This paper is structured as follows. In Sec. II, we present the probe characteristics for shot 141 899 with both HHFW and NB power. Despite SOL turbulence, effects consistent with RF rectification are observed in the characteristics. In Sec. III, the fundamental equations of RF rectification are reviewed, and a formula for the heat flux across a sheath in the presence of an RF electric field is derived. These equations are then applied to NSTX data from Sec. II, demonstrating a consistent picture in which RF rectification is playing a substantial role in the RF losses under the heat spiral. In Sec. IV, we show the RF effects on the probe characteristics for a shot with HHFW power alone for which turbulence effects on the probe signals are reduced and for which the RF rectification effects are more clearly observed. Section V contains discussion of the results and the steps to be taken on NSTX-U to permit more quantitative evaluations of the RF rectification contribution to the SOL losses.

II. PROBE CHARACTERISTICS FOR THE CASE WITH BOTH HHFW AND NB POWER

Shot 141 899, with 1.3 MW of applied HHFW power and 2 MW of NB power, provides a good opportunity to study the influence of the applied RF power on the Langmuir probes, as the magnetic field for this shot places the heat spiral over the outermost probe of the array (probe 4, P4) but not over probe 2 (P2) just 6 cm inboard. This claim is substantiated by the strong effect of the applied RF on the floating potential of probe 4, V_{fp4} , and the relatively small effect on the floating potential of probe 2, V_{fp2} (Fig. 3); also, the computed location at 433 ms (Fig. 2(b)) lies squarely over P4 but not P2.¹⁴ This shows that the RF losses to the divertor via the SOL are confined primarily to the spiral, which permits comparison of probe characteristics both with and without RF under nearly identical plasma conditions. The equilibrium reconstruction for this shot also indicates that the angle between the magnetic field and the normal of the probe surfaces is quite similar: 86.1° for P2 and 85.1° for P4.

The primary effect of RF rectification is either (1) to drive an enhanced electron current to the surface or (2) for surfaces which are floating (e.g., draw no net current), to drive the floating potential more negative to offset the enhanced electron current.¹⁹ This happens whether the RF voltage is applied through the probe bias voltage as in Ref. 19 or, as is the present case, if the RF oscillations originate in the plasma.²⁸ The fast negative response of the floating potential V_{fp4} to the applied RF power is thus consistent

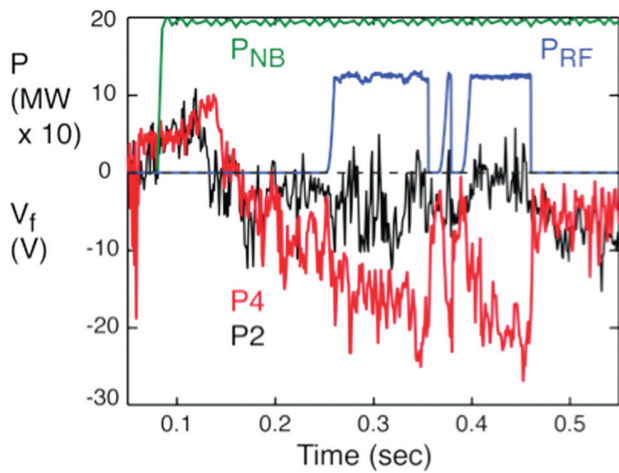


FIG. 3. Floating potentials for probes 2 and 4 for shot 141 899 (from Ref. 14). The spiral lies over probe 4 (P4) but not probe 2 (P2). Reprinted with permission from R. J. Perkins *et al.*, Phys. Rev. Lett. **109**, 045001 (2012). Copyright 2012 American Physical Society.¹⁴

with RF rectification, as are the currents to the probes at ground potential ($V_{pr} = 0$): the electron current to probe 4 is enhanced, while probe 2 is little effected. This is shown in Fig. 4(a), where the current to the probe is plotted for probe bias voltages close to 0 V (between -0.5 V and $+0.5$ V, potentials relative to vessel potential). This response to the RF is very similar to that found on the tile currents with the electron current being enhanced for the tile under the spiral

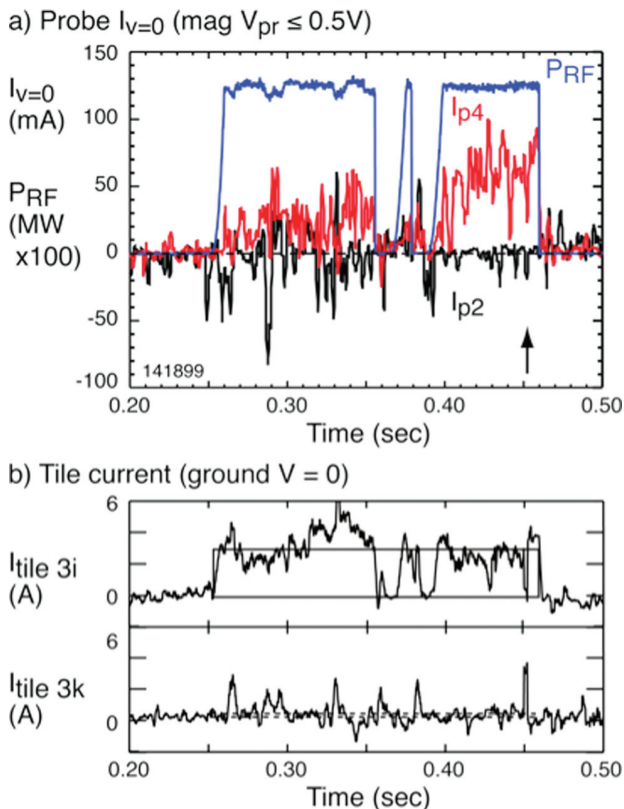


FIG. 4. (a) I_{pr} for probes 4 and 2 at $V_{pr} = 0$ (vessel potential) and (b) tile 3i and 3k currents. The probe and tile under the spiral show significant current away from them (electron current collection).

(tile 3i of Fig. 4(b)) but not from tiles away from the spiral (tile 3k of Fig. 4(b)). See Fig. 2(a) for the locations of the tiles relative to the spiral.

To further investigate the role of RF rectification, the probe IV characteristics for probes 2 and 4 taken with 1 ms voltage sweeps starting at $t = 0.4515$ s are shown in Fig. 5. It is immediately clear that for the same bias voltage, probe 4 draws more electron current than probe 2, and its floating potential (the intersection of the IV characteristic with the $I = 0$ axis) has shifted to a more negative value. These observations are consistent with RF rectification but could also result from plasma heating, and the large fluctuations in probe current due to the turbulent conditions in the periphery of the discharge make it difficult to discern the underlying cause. For probe 2, an exponential fit is made in the vicinity of the floating potential with $I_{sat} = 6$ mA, $V_{fl} = 0$ V, and $T_e = 13$ eV. Discussion of the fit functions can be found in Sec. III. For probe 4, two potential choices for exponential fits are shown. The first exponential (red curve) is for $I_{sat} = 10$ mA, $V_{fl} = -30$ V, $T_e = 15$ eV; this exponential fits the data with $V_{pr} < 18$ V well. For $V_{pr} > 18$ V, we presume for this fit that electron collection is saturated (dashed line in Fig. 5) due to the grazing-incident magnetic field (this will be discussed in Sec. III), and the positive swing of V_{RF} reaches the non-exponential (saturated) part of the characteristic without the presence of RF. The large change in floating potential with little change in electron temperature is suggestive of RF rectification. The second exponential (blue curve) has $I_{sat} = 60$ mA, $V_{fl} = -25$ V, and $T_e = 31$ eV over the entire voltage range, indicative of plasma heating. It is difficult to choose between the two fits for this single sweep case. In order to average over the turbulence, six consecutive 1 ms voltage sweeps beginning at $t = 0.4515$ s are averaged together giving the characteristics shown in Fig. 6. With a reduced fluctuation level, exponentials with the same ion saturation current and electron temperature but different floating potentials give relatively good fits for both probe characteristics in the vicinity of the floating potential for both probes. Again, this is as expected for RF rectification

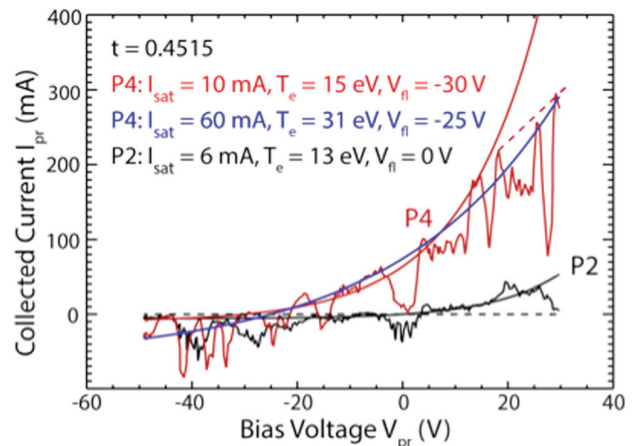


FIG. 5. IV characteristics for probes 2 and 4 at 0.4515 s (arrow in Fig. 4(a)). Turbulence at divertor plate makes it difficult to choose the red exponential fit (RF rectification) or the blue exponential fit (plasma heating) for P4 (underneath spiral).

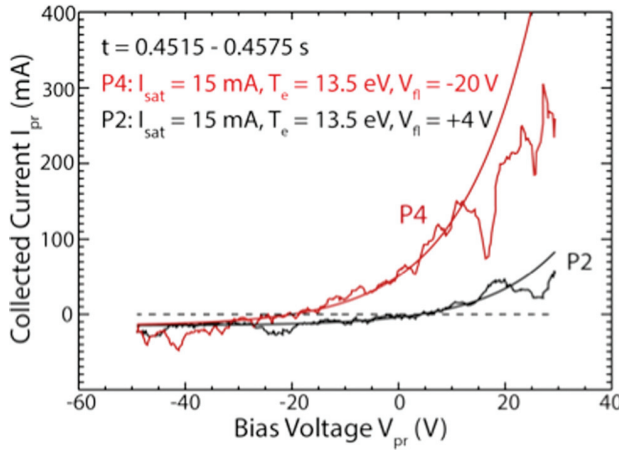


FIG. 6. IV characteristics for probes 2 and 4 averaged over six consecutive voltage sweeps starting at 0.4515 s. The exponential fits for probes 2 and 4 have the same I_{sat} and T_e , but different V_{fl} values, indicative of RF rectification.

for which only the floating potential is affected¹⁹ in the exponential ranges of the characteristics.

The temperature that best fits the probe characteristics in Fig. 6, $T_e = 13.5$ eV, compares well with Thomson scattering measurements at the SOL mid-plane. In Fig. 7, the temperature obtained from the IV characteristics, T_{eIV} , is compared to two temperature profiles measured with Thomson scattering at the two times prior to the end of the RF pulse. The probe midplane positions (major radii) are defined by the field lines connecting the probes to the midplane. It is clear that $T_{eIV} = 13.5$ eV is in reasonable agreement with the Thomson scattering temperatures at these midplane probe locations. Also plotted is $T_e = 31$ eV, the hotter electron temperature that fits the probe 4 characteristic reasonably well in Fig. 5 (blue exponential). This hotter electron temperature compares far less favorably with the Thomson scattering data, which furthers the case for RF rectification. It should be noted that the Thomson scattering data are obtained at Bay F outside the field line bundle linking the spiral.

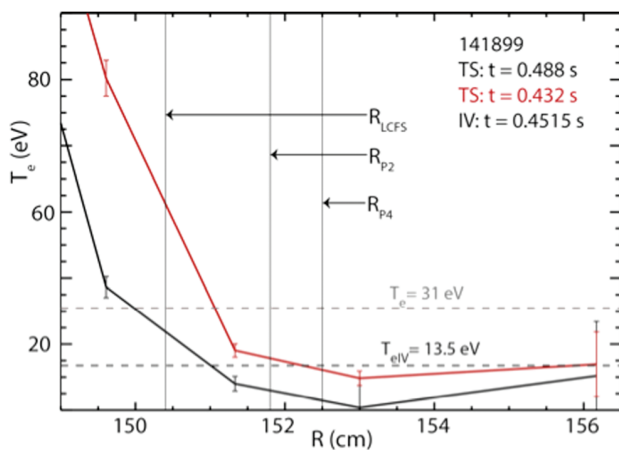


FIG. 7. The electron temperature determined from the probe characteristics ($T_e = 13.5$ eV, Fig. 6) is in reasonably good agreement with Thomson scattering measurements at the midplane. Probes 2 and 4 map along field lines to $R = 151.8$ cm and 152.5 cm at the midplane, and the LCFS midplane radius is 150.4 cm.

III. RF RECTIFICATION AND RF HEAT FLUX TRANSMISSION AT A SHEATH

This section reviews the fundamental equations for Langmuir probes and RF rectification. The average sheath heat flux transmission factor in the presence of an RF field is derived and is shown to be substantially greater than the transmission factor with no RF. The equations presented here are used to estimate the amplitude of the RF voltage and the heat deposition due to RF fields onto the divertor region of NSTX.

A. RF rectification

For a Maxwellian electron distribution function, the IV characteristic of a Langmuir probe biased below the plasma potential exhibits exponential behaviour for sufficiently negative bias voltage so that the magnetic field is not affecting the electron current to the probe.²⁹ In the exponential region,

$$I_{pr}(V) = I_{\text{sat}} [-1 + \exp((V - V_{fpl})/T_e)], \quad (1)$$

where V is the probe bias, I_{sat} is the ion saturation current, V_{fpl} is the floating potential relative to plasma potential (as opposed to the vessel potential), and T_e (eV) $\equiv kT_e$ ($^{\circ}\text{K}$)/ e here. V_{fpl} is given by,³⁰ [Eq. 25.31]

$$\frac{V_{fpl}}{T_e} = \frac{1}{2} \ln \left[2\pi \frac{m_e}{m_i} \left(1 + \frac{T_i}{T_e} \right) (1 - \delta_e)^{-2} \right], \quad (2)$$

with δ_e being the secondary electron emission coefficient. It is the non-linear nature of this IV characteristic that gives rise to RF rectified effects; upon adding a sinusoidal potential to the probe bias, the probe will draw more electron current on the positive excursion of this oscillating potential than it will on the negative excursion. Again, it does not matter whether the RF potential is added to the probe bias or to the plasma potential; it is the resulting voltage across the sheath that matters. If the probe potential always remains in the range over which the IV characteristic exhibits exponential behaviour and the sheath thickness does not vary significantly with RF potential, then the average current can be computed using the relation³¹ [Eq. 9.6.16]

$$I_0(z) = \frac{1}{\pi} \int_{-\pi/2}^{\pi/2} e^{z \sin \theta} d\theta, \quad (3)$$

with I_0 being the modified Bessel function of order zero. Expressing V as the sum of a bias voltage and a sinusoidal potential, e.g., $V \rightarrow V + V_{\text{RF}} \sin(\omega t)$, and averaging over an RF cycle, the average current drawn by the probe is

$$I_{pr}^{\text{ave}}(V) = I_{\text{sat}} \left[-1 + I_0 \left(\frac{V_{\text{RF}}}{T_e} \right) \exp((V - V_{fpl})/T_e) \right]. \quad (4)$$

Since $I_0(x) > 1$ for all x , the electron current drawn by the probe is enhanced for a given probe bias, as is observed on the current-measuring tile 3i in Fig. 4(b) and on probe 4 in Figs. 4(a) and 6. The floating potential with RF, V_{flRF} , is the probe bias voltage at which no net current is drawn by the probe: $I_{pr}^{\text{ave}} = 0$ in Eq. (4):¹⁹

$$\exp((V_{flpl} - V_{fIRF})/T_e) = I_0(V_{RF}/T_e), \quad (5)$$

where V_{flpl} remains the floating potential in the absence of V_{RF} .

We can now apply Eq. (5) to get an estimate of the RF voltage at the sheath for probe 4. In Fig. 6, $V_{flpl} - V_{flRF} = V_{flP2} - V_{flP4} = 4 \text{ V} + 20 \text{ V} = 24 \text{ V}$. Then, with $T_e = 13.5 \text{ eV}$, the value of V_{RF} is 43.7 V.

B. Average RF heat flux transmission

We can similarly quantify the average of the heat flux through a sheath to a surface in the presence of an RF field. The heat flux to a surface is

$$q_s = \gamma T_e J_{sat}, \quad (6)$$

where γ is the sheath transmission factor. γ has been computed from first-principles³⁰ [Eq. 25.54] in the absence of RF fields to be

$$\gamma(V) = -\frac{V}{T_e} + 2.5 \frac{T_i}{T_e} + 2 \sqrt{2\pi \frac{m_e}{m_i} \left(1 + \frac{T_i}{T_e}\right)} \exp\left(\frac{V}{T_e}\right). \quad (7)$$

Again, the voltages in Eq. (7) are defined relative to plasma potential, but the probe measurements are relative to the vessel potential. To express Eq. (7) in voltages measured by the probe, define $V = V_{flpl} + \Delta V$, so that Eq. (7) can be rewritten using Eq. (2) to give

$$\gamma(V) = -\frac{V_{flpl}}{T_e} - \frac{\Delta V}{T_e} + 2.5 \frac{T_i}{T_e} + \frac{2}{1 - \delta_e} \exp\left(\frac{\Delta V}{T_e}\right). \quad (8)$$

The heat flux to the probe at vessel potential, $V_{pr} = 0$, is also the heat flux delivered to the surrounding divertor tiles. Let V_{fl0} denote the floating potential relative to the vessel potential without RF; then at ground potential, $\Delta V = -V_{fl0}$. This gives

$$\gamma_{noRF} = -\frac{V_{flpl}}{T_e} - \frac{V_{fl0}}{T_e} + 2.5 \frac{T_i}{T_e} + \frac{2}{1 - \delta_e} \exp\left(-\frac{V_{fl0}}{T_e}\right). \quad (9)$$

With RF applied, we add an oscillating potential, $\Delta V = -V_{fl0} + V_{RF} \sin(\omega t)$, and average γ over an RF cycle as in Eq. (3) to give

$$\gamma_{RF}^{ave} = -\frac{V_{flpl}}{T_e} - \frac{V_{fl0}}{T_e} + 2.5 \frac{T_i}{T_e} + \frac{2}{1 - \delta_e} I_0\left(\frac{V_{RF}}{T_e}\right) \exp\left(-\frac{V_{fl0}}{T_e}\right). \quad (10)$$

Using Eq. (5) from above with the floating potentials relative to ground, $V_{flRF} \rightarrow V_{flRF0}$ and $V_{fl} \rightarrow V_{fl0}$,

$$\gamma_{RF}^{ave} = -\frac{V_{flpl}}{T_e} - \frac{V_{fl0}}{T_e} + 2.5 \frac{T_i}{T_e} + \frac{2}{1 - \delta_e} \exp\left(-\frac{V_{flRF0}}{T_e}\right). \quad (11)$$

This equation can give a substantial increase in γ and hence in the incident heat flux with an RF field added.

It should be noted that these equations only apply if the probe voltage (bias plus RF) remains in the range in which the IV characteristic without RF is exponential. For unmagnetized plasma, the IV characteristic can remain exponential up to the plasma potential, but for magnetized plasma intercepting a material surface at an oblique angle, deviation from exponential behaviour will occur at lower probe voltages.^{29,32}

For the IV characteristics in Fig. 6 and taking probe 2 to be the no RF case and probe 4 as the RF case, we have $V_{fl0} = V_{flP2} = 4 \text{ V}$, and $V_{flRF0} = V_{flP4} = -20 \text{ V}$ as well as $T_e = 13.5 \text{ eV}$ and $I_{sat} = 15 \text{ mA}$. Using Eqs. (10) and (11) with the assumption at first that $T_i = T_e$ gives

$$\gamma_{P2} = 7.12 \quad \gamma_{P4} = 14.43.$$

With probe dimensions of $2 \text{ mm} \times 7 \text{ mm}$,¹⁶ we obtain using Eq. (6)

$$q_{P2} = 0.103 \text{ MW/m}^2 \quad q_{P4} = 0.209 \text{ MW/m}^2.$$

Thus, the applied RF power for the case of Sec. II is predicted to double the heat flux to the probe (and tiles) at the probe location at Bay B (Figs. 1 and 2).

A measurement of the ion temperature made with the edge rotation diagnostic (ERD)^{33,34} is shown in Fig. 8 for $t = 0.450 \text{ s}$ for shot 141 899. This temperature is for carbon (CIII) in the edge of the plasma and approximately equals T_e at $R = 150 \text{ cm}$. A T_i measurement at the P4 position, as extrapolated to the mid-plane along a field line, is not available, but the assumption above that $T_i = T_e$ above would appear to be not unreasonable. However, T_e and T_i are expected to be decoupled in the SOL, and, to indicate the dependence of heat flux values on T_i/T_e , we consider the γ values at $T_i/T_e = 2$:

$$\gamma_{P2} = 9.42 \quad \gamma_{P4} = 16.73,$$

and q increases to

$$q_{P2} = 0.136 \text{ MW/m}^2 \quad q_{P4} = 0.242 \text{ MW/m}^2.$$

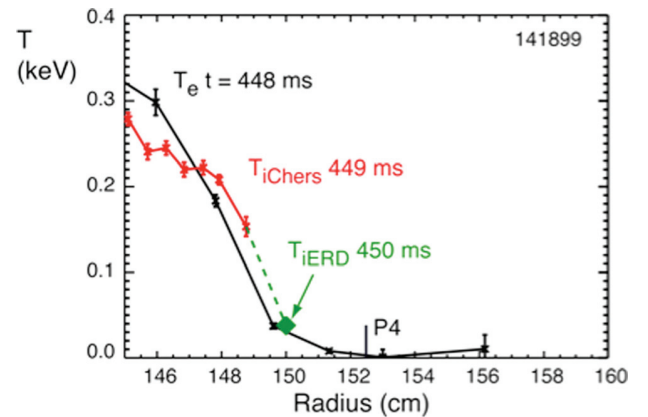


FIG. 8. Edge rotation diagnostic measurement of the toroidal T_i (CIII) at 0.450 s and T_i Chers measurement T_i (CVI) at 0.449 s compared to T_e at 0.448 s. The vertical line is the extrapolated probe 4 position at the mid-plane.

The background flux increases by $\sim 30\%$ and the increase with RF remains at $\sim 0.1 \text{ MW/m}^2$.

IR camera measurements are not available at the probe location (Bay B), but it is of interest to compare the probe heat flux calculations above to projections based on IR camera heat flux measurements at Bay I bottom and Bay G top (see Fig. 1).¹² Both IR camera measurements, taken at times just prior to the time of the probe data, are shown in Fig. 9 for shot 141 899; the blue curves indicate heat flux profiles with no applied RF power, black curves indicate profiles with RF power, and the red curves indicating the difference δQ . The dip in heat flux around $R = 0.6 \text{ m}$ is due to the vessel gap. For the Bay I measurement (Fig. 9(a)), the first (outermost) pass of the spiral across Bay I occurs between $R = 0.9$ and 1.0 m (the apparent two-peak structure is due to a “notch” in the heat flux caused by tile structure). The spiral makes a second pass across Bay I just inboard of the vessel gap, around $R = 0.59 \text{ m}$. The probes are located just outside the vessel gap (gap center at $R \sim 0.6 \text{ m}$) with the probe 4 radial position indicated by an arrow. Around this probe radial position, the background heat flux at Bay I is roughly 0.3 MW/m^2 , which is roughly twice the values for q_{P2} computed above. To get a sense for the heat flux underneath the spiral, we look to the second spiral pass. At this position, close to the outer vessel strike radius (OVSR), there are two

contributions to the RF-produced heat flux δQ : the direct loss of RF power in the SOL, and the plasma exhaust of RF heat coupled to the core. It is difficult to disentangle the two effects, especially as heat flux measurements are not available at smaller major radii for this shot due to hardware issues. The dashed line in Fig. 9(a) indicates a rough guess for the RF-produced increment in plasma exhaust; the increment in δQ above this dashed line then indicates the heat flux for the second spiral pass at Bay I, about 0.3 MW/m^2 . This is about three times greater than the increment $q_{P4} - q_{P2}$ computed above; however, this increment is observed to decrease as the second pass is moved to the region outside the gap by decreasing the magnetic field pitch in the SOL.³⁵ Lastly, we consider the IR measurements at Bay G top, where the first pass is located outboard of the vessel gap at a major radius close to the probe radii and exhibits a background of $\sim 0.2 \text{ MW/m}^2$ and an increment due to the RF of $\sim 0.1 \text{ MW/m}^2$. These values are closer to those calculated from the IV characteristics. It is apparent that precise quantitative comparisons are not yet possible due primarily to physical separation of the measurement locations and the strong variation in spiral intensity along the length of the spiral (as described in Ref. 35). Also, there are the known difficulties in obtaining strict quantitative agreement between heat fluxes computed from probe data and IR thermography³⁶ [references therein]. Qualitatively, though, these IR measurements indicate that the heat flux values calculated from the IV characteristics are within a factor of two for the background, and thus a substantial part of the heat flux increment with RF is due to RF rectification as presented here. Diagnostic improvements to be found on NSTX-Upgrade will allow for more rigorous comparison and will be discussed in Sec. V.

IV. PROBE CHARACTERISTICS FOR THE P_{RF} ONLY CASE

Without neutral beam injection and only RF power applied, the turbulence in the plasma edge is reduced substantially and IV characteristics with reduced fluctuation levels in the probe current are obtained. Here, we consider probe characteristics for shot 141 836 with $P_{\text{RF}} = 1.1 \text{ MW}$, $B_T = 5.5 \text{ kG}$, $I_p = 0.65 \text{ MA}$, and helium. The SPIRAL code is again used to compute the location of the field line strike points on the lower divertor for lines passing in front of the antenna as shown in Fig. 10. At this lower pitch relative to the case of Fig. 2, the spiral is rotated clockwise so that the second pass of the spiral no longer intercepts the probes at Bay B and the first pass now falls on tiles 4k and 4a outboard of tiles 3i and 3k. For this condition, the spiral now intercepts probe 1 and misses probe 3 as indicated by the floating potential measurements in Fig. 11. Here, the field angles for the probes are again quite similar: angles are P1 88.6° and P3 88.3° . Again the negative shift of the floating potential with RF applied indicates that RF rectification is likely present. Note that the floating potential for P1 reverses sign before the end of the RF power pulse as caused by the OVSR passing over the probe.^{16,37} We will examine the IV

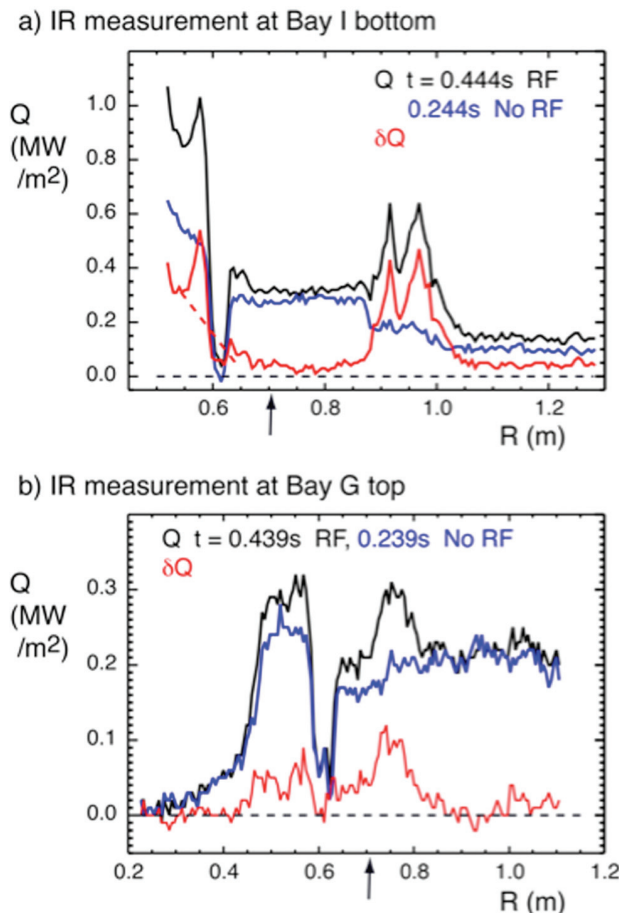


FIG. 9. IR power deposition measurements for (a) Bay I bottom and (b) Bay G top (see Fig. 1). The radial location of probe 4 is indicated by arrows.

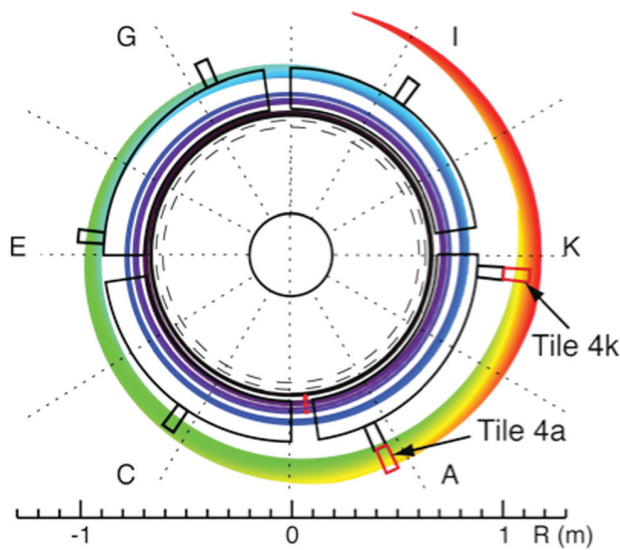


FIG. 10. Calculated spiral location on lower divertor for field lines passing in front of the HHFW antenna at $t = 350$ ms for shot 141 836. Color signifies the radial location of the line in the SOL: red is near the antenna and black is near the LCFS. Plasma conditions are $B_T = 5.5$ kG, $I_p = 0.65$ MA (magnetic pitch in the SOL $\sim 27^\circ$), $P_{RF} = 1.1$ MW, $P_{NB} = 0$, and helium.

characteristics at $t \sim 0.362$ s, where the OVSR is sufficiently far from the probe so as to not affect the floating potential.

The currents to probes while at ground potential ($V_{pr} = 0$) and the currents for tiles 4k and 4a are given in Fig. 12 versus time. $I_{V=0}$ for P1 responds to the applied RF pulse as did P4 in Fig. 4, and tiles 4k and 4a now respond to the RF pulse as anticipated from Fig. 10, which places the spiral over these tiles. Note that the plasma is gradually moving outward for this case as evidenced by the probe 1 V_{fl} and $I_{V=0}$ going through zero at $t = 0.397$ s in Figs. 11 and 12(a) as the OVSR passes over probe 1.³⁷

The IV characteristics for probes 1 and 3, averaged over six consecutive 1 ms voltage sweeps starting at 0.362 s, are shown in Fig. 13. The characteristics exhibit much smaller current fluctuations than those of Fig. 6, and the exponential character of the probe 3 curve is much better defined. The exponential fits to the characteristics in the vicinity of the floating potentials with the same I_{sat} and T_e but with different floating potentials are quite good. We apply Eq. (5) to get an estimate of the RF voltage at the sheath for probe 1. From

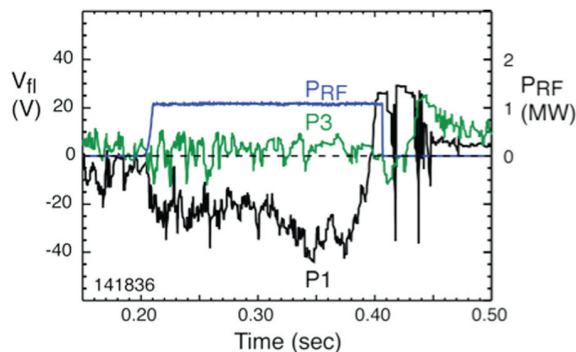
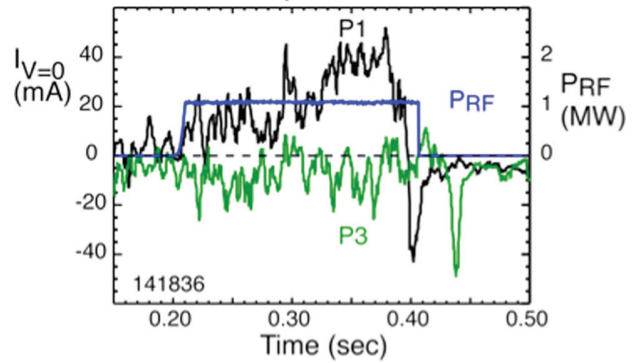


FIG. 11. Floating potentials for probes 1 and 3 for shot 141 836. Spiral lies over probe 1 (P1).

a) Probe $I_{V=0}$ ($\text{mag } V_{pr} \leq 0.5$ V)



b) Tile current (ground $V = 0$)

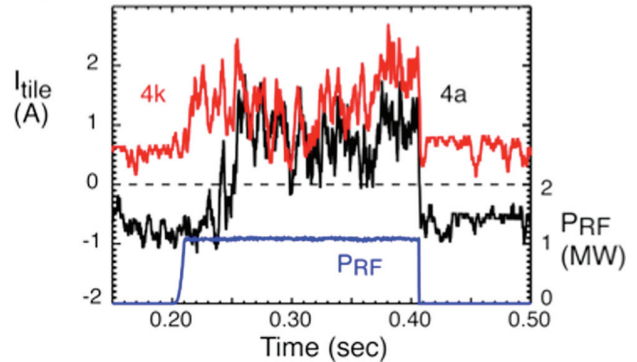


FIG. 12. (a) I_{pr} for probes 1 and 3 at $V_{pr} = 0$ (vessel potential) and (b) tile 4a and 4k currents. The probe and tiles under the spiral show significant current away from them (electron current collection) during RF heating.

Fig. 13, $V_{fl} - V_{flRF} = V_{flP3} - V_{flP1} = 5.5$ V + 28 V = 33.5 V. Then, with $T_e = 34$ eV, the value of V_{RF} is 75.7 V. The common T_e in this case is 34 eV, which is considerably higher than that for Fig. 6 for the RF + NBI case. However, this value is in relatively good agreement with Thomson scattering measurements at the midplane (Fig. 14), which are also much larger than the values in Fig. 7 at the indicated radial midplane probe locations. Note that the probe locations mapped to the mid-plane are very close to the LCFS as suggested in Figs. 10 and 14.³⁷

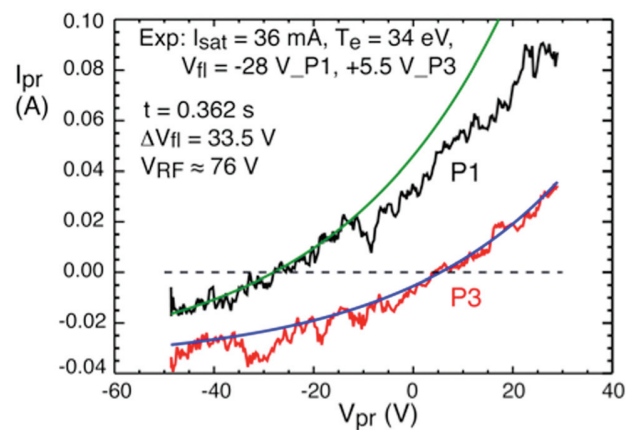


FIG. 13. Probe IV characteristics for probes 1 and 3 averaged over six consecutive voltage sweeps starting at 0.362 s. Exponential fits for probes 1 and 3 have the same I_{sat} and T_e , but different V_{fl} values.

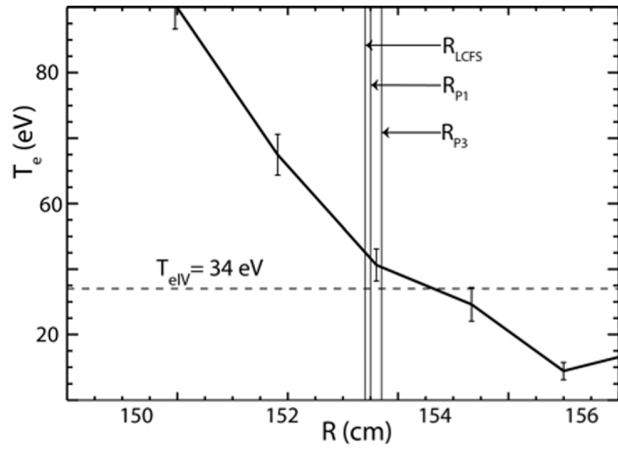


FIG. 14. Probe T_e at 0.362 s is in reasonably good agreement with Thomson scattering T_e measurements at the plasma midplane at 0.365 s. Probes 1 and 3 map long field lines to $R = 149.05$ cm and 149.26 cm, and LCFS midplane radius is 149.00 cm.

The outward movement of the OVSR complicates the comparison of the heat fluxes to the probe with IR camera measurements. However, it is worth making the comparison to assure that the calculated fluxes for the probe are still in the approximate range of the IR camera measurements. Assuming the ion charge $Z = 2$ in this helium case, we modify the term $(1 + T_i/T_e) \Rightarrow (Z + T_i/T_e)$ in Eq. (2) and $2.5 T_i/T_e \Rightarrow (2.5 T_i/T_e)/Z$ in Eqs. (8) and (11).³⁸ Then for the exponentials of Fig. 13 with $T_e = 34$ eV, $I_{\text{sat}} = 36$ mA, $V_{\text{flP1}} = -28$ V, $V_{\text{flP3}} = +5.5$ V, and $T_i = T_e$,

$$\gamma_{P1} = 6.62 \quad \gamma_{P3} = 5.20,$$

$$q_{P1} = 0.579 \text{ MW/m}^2 \quad q_{P3} = 0.454 \text{ MW/m}^2$$

$$q_{P1} - q_{P3} = 0.125 \text{ MW/m}^2.$$

The value of q_{P1} should be slightly reduced by the saturation effect of the electron current by $\sim 10\%$ from the exponential at $V_{P1} = 0$ (Fig. 13, (Ref. 38)).

The IR camera measurements taken in the vicinity of Bay I for $t = 0.352$ s are shown in Fig. 15. There is no

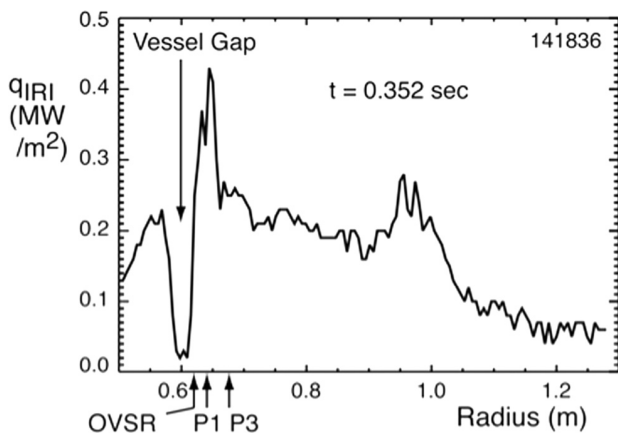


FIG. 15. IR power deposition measurements for Bay I bottom (see Fig. 1). The midplane radial location of the OVSR, probes 1 and 3 are indicated by arrows.

subtraction to obtain δQ due to the motion of the plasma. The heat flux profile would shift outward at the later time of the probe characteristics (0.362–0.368 s) due to the plasma motion, but the radial position of the spiral passes would shift inward as one moves around the torus to the probe positions at Bay B. Figure 15 shows two peaks outside the vessel gap as has been observed for the spiral passes close to the OVSR earlier.³⁵ The increment in heat flux under the RF spiral in the vicinity of probe 1 is somewhere between 0.12 and 0.18 MW/m^2 depending on the exact location of the peaks relative to the probe. However, the background calculated q_{P3} is a factor of ~ 1.8 larger than the IR camera measurement at its location. Again, these comparisons indicate that the calculated contribution of RF rectification to the heat flux to the divertor under the RF heat flux spiral could very well be within the range measured via IR thermography. However, quantitative comparisons must await HFW operations on NSTX-U for which the probe and IR camera measurements will be co-located.

It is of interest to determine if the calculated V_{RF} depends on the applied RF power. In Fig. 16, the probe characteristics at $t = 0.294$ s for the helium shot with $P_{\text{RF}} = 1.1$ MW (shot 141836 in Fig. 11) are compared with the probe characteristics at $t = 0.294$ s for a helium shot with $P_{\text{RF}} = 0.55$ MW (shot 141830). The earlier time is chosen for the comparison since at the lower power, the outer vessel strike radius moved out faster and crossed over probe 1 at $t = 0.34$ s.³⁷ The V_{RF} found

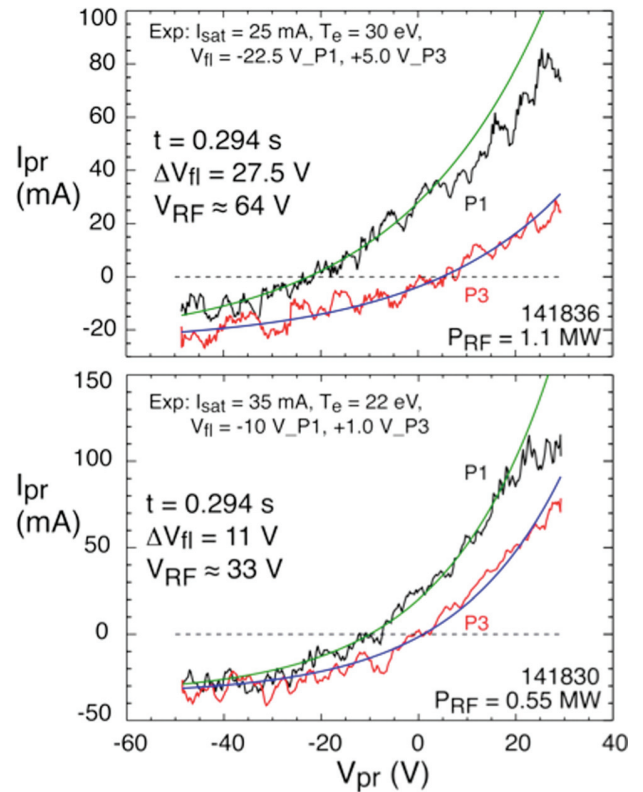


FIG. 16. IV characteristics for (a) $t = 0.294$ s for shot 141836 ($P_{\text{RF}} \approx 1.1$ MW) and for (b) $t = 0.294$ s for shot 141830 ($P_{\text{RF}} \approx 0.55$ MW). Exponential fits for P1 and P3 have the same I_{sat} and T_e for each case, with ΔV_{fl} as noted. The plasma conditions for shot 141836 are in the caption of Fig. 10 and those for shot 141830 are the same except that $P_{\text{RF}} = 0.55$ MW.

for this earlier time for the $P_{\text{RF}} = 1.1$ MW case is 64 V, a value somewhat smaller than for the later time in Fig. 13, possibly because the probes are farther away from the OVSR at the earlier time (P1 maps along the field line to 5 mm outside the LCFS as compared to 1 mm outside for the later time). At the reduced power of $P_{\text{RF}} = 0.55$ MW, V_{RF} is found to be 33 V (P1 maps along the field line to 3 mm outside the LCFS in this case). The ratio of $P_{\text{RF}} = 1.1/0.55$, and one might expect V_{RF} to scale as $\sqrt{P_{\text{RF}}}$ for the same plasma conditions. Here, the ratio of V_{RF} is found to be $64/33 = 1.9$, slightly larger than the anticipated value of $\sqrt{2} \sim 1.4$. Of course, the plasma conditions are changing with RF power as evidenced by the different I_{sat} and T_e values obtained and thus the change in V_{RF} with P_{RF} is quite reasonable. Note that comparing V_{RF} between shots 141 836 and shots 141 899 (a deuterium discharge with a larger outer gap as was necessary for neutral beam injection) is not feasible as the edge conditions are too disparate.

V. CONCLUSIONS AND DISCUSSION

The IV characteristics for probes spaced relatively close to each other, one located under the RF heat spiral and the other located outside the spiral zone, permit comparisons without shot to shot variations. The effect of the RF on the characteristic is well represented by a negative shift in floating potential for the same exponential parameters— T_e and I_{sat} . The shift is clear for both the RF and NBI case as well as the RF-only case; however, plasma turbulence requires that several 1 ms voltage sweeps be averaged to highlight this shift. T_e values obtained from the IV characteristics compare favorably with the mid-plane Thomson scattering T_e measurements, which further support RF rectification as the primary effect over parasitic SOL plasma heating. The negative shift in probe voltage with RF applied leads to the specification of the RF voltage across the probe sheath as (a) $V_{\text{RF}} = 43.7$ V for $P_{\text{RF}} = 1.3$ MW with $P_{\text{NB}} = 2$ MW, and (b) $V_{\text{RF}} = 75.7$ V for $P_{\text{RF}} = 1.1$ MW. Thus, the hypothesis that RF rectification is largely responsible for the response of divertor diagnostics underneath the spiral is consistent with the data, implying that direct plasma heating in the SOL by the RF waves may be minimal and not contributing significantly to the heat flux at the RF heat spiral.

We hypothesize that the heat flux increment in the spiral is also associated primarily with RF rectification in that the increase in the electron current at ground potential enhances the sheath transmission factor. This increment is ~ 0.1 MW/m² at the probe location as calculated for the case of RF and NBI using the RF-averaged sheath transmission factor, γ_{RF} , of Eq. (11). For the amplitude of V_{RF} found here, γ_{RF} is substantially larger than the usual sheath transmission factor that does not take into account the presence of V_{RF} . Although not measured at the probe location, IR camera measurements of the spiral heat flux at other toroidal locations show that 0.1 MW/m² is in the expected range for the heat flux increment at the probe location.

Based on the above results, the objective on NSTX-U will be to quantify further the RF rectification contribution to the RF heat flux spiral and determine its relative contribution to the total RF power lost in the SOL. Specifically, we will

measure (1) the amplitude of the RF voltage at the location where we anticipate the spiral being most intense, (2) the heat flux at the probe locations via IR thermography, and (3) the total heat flux delivered to the divertor regions by the spiral. The RF voltages will be measured with a new radial array of Langmuir probes located at port J, one bay clockwise from Bay I in Fig. 1, where the brightest (hottest) part of the spiral should lie.³⁹ The probes are equipped with coaxial line suitable for RF measurements, and the RF (30 MHz) component of the probe voltages should be easily measurable to directly obtain V_{RF} . A wide-view IR camera will measure the heat flux at the probe location at Bay J and also the total heat flux under the spiral, allowing us to verify that the measured RF voltages are sufficiently large to produce the measured heat flux in the spiral, and that this total heat flux accounts for a significant fraction of the RF power missing from the core. Furthermore, the probe measurements will allow for comparisons between the measured V_{RF} to that predicted from applying the AORSA code¹³ to calculate $E \parallel B$ and V_{RF} at the probe locations, and similarly using the RF sheath boundary formalism.⁴⁰ This will both help quantify the RF rectification contribution to the heat flux under the spiral and help to determine the heat flux due to RF heating in the SOL prior to the waves intercepting the spiral, if any.

ACKNOWLEDGMENTS

The authors wish to acknowledge the support of Dr. Masayuki Ono and Dr. Jonathan Menard, the NSTX team and the machine, RF, and neutral beam operations groups. This work is supported by USDOE Contract No. DE-AC02-09CH11466.

¹D. W. Swain and R. H. Goulding, *Fusion Eng. Des.* **82**, 603 (2007).

²M. Ono, *Phys. Plasmas* **2**, 4075 (1995).

³C. E. Kessel, E. J. Synakowski, M. E. Bell, D. A. Gates, R. W. Harvey, S. M. Kaye, T. K. Mau, J. Menard, C. K. Phillips, G. Taylor, R. Wilson, and the NSTX Research Team, *Nucl. Fusion* **45**, 814 (2005).

⁴D. Liu, W. W. Heidbrink, M. Podestà, R. E. Bell, E. D. Fredrickson, S. S. Medley, R. W. Harvey, and E. Ruskov, *Plasma Phys. Controlled Fusion* **52**, 025006 (2010).

⁵M. Podestà, R. E. Bell, E. D. Fredrickson, N. N. Gorelenkov, B. P. LeBlanc, W. W. Heidbrink, N. A. Crocker, S. Kubota, and H. Yuh, *Phys. Plasmas* **17**, 122501 (2010).

⁶E. D. Fredrickson, G. Taylor, N. Bertelli, D. S. Darrow, N. Gorelenkov, G. Kramer, D. Liu, N. A. Crocker, S. Kubota, and R. White, *Nucl. Fusion* **55**, 013012 (2015).

⁷M. Ono, S. M. Kaye, Y.-K. M. Peng, G. Barnes, W. Blanchard, M. D. Carter, J. Chrzanowski, L. Dudek, R. Ewig, D. Gates, R. E. Hatcher, T. Jarboe, S. C. Jardin, D. Johnson, R. Kaita, M. Kalish, C. E. Kessel, H. W. Kugel, R. Maingi, R. Majeski, J. Manickam, B. McCormack, J. Menard, D. Mueller, B. A. Nelson, B. E. Nelson, C. Neumeyer, G. Oliaro, F. Paoletti, R. Parsells, E. Perry, N. Pomphrey, S. Ramakrishnan, R. Raman, G. Rewoldt, J. Robinson, A. L. Roquemore, P. Ryan, S. Sabbagh, D. Swain, E. J. Synakowski, M. Viola, M. Williams, J. R. Wilson, and NSTX Team, *Nucl. Fusion* **40**, 557 (2000).

⁸J. Hosea, R. E. Bell, B. P. LeBlanc, C. K. Phillips, G. Taylor, E. Valeo, J. R. Wilson, E. F. Jaeger, P. M. Ryan, J. Wilgen, H. Yuh, F. Levinton, S. Sabbagh, K. Tritz, J. Parker, P. T. Bonoli, R. Harvey, and NSTX Team, *Phys. Plasmas* **15**, 056104 (2008).

⁹J. C. Hosea, R. E. Bell, E. Feibush, R. W. Harvey, E. F. Jaeger, B. P. LeBlanc, R. Maingi, C. K. Phillips, L. Roquemore, P. M. Ryan, G. Taylor, K. Tritz, E. J. Valeo, J. Wilgen, J. R. Wilson, and NSTX Team, *AIP Conf. Proc.* **1187**, 105 (2009).

- ¹⁰C. K. Phillips, R. E. Bell, L. A. Berry, P. T. Bonoli, R. W. Harvey, J. C. Hosea, E. F. Jaeger, B. P. LeBlanc, P. M. Ryan, G. Taylor, E. J. Valeo, J. B. Wilgen, J. R. Wilson, J. C. Wright, H. Yuh, and NSTX Team, *Nucl. Fusion* **49**, 075015 (2009).
- ¹¹G. Taylor, R. E. Bell, J. C. Hosea, B. P. LeBlanc, C. K. Phillips, M. Podesta, E. J. Valeo, J. R. Wilson, J.-W. Ahn, G. Chen, D. L. Green, E. F. Jaeger, R. Maingi, P. M. Ryan, J. B. Wilgen, W. W. Heidbrink, D. Liu, P. T. Bonoli, T. Brecht, M. Choi, and R. W. Harvey, *Phys. Plasmas* **17**, 056114 (2010).
- ¹²D. Mastrovito, R. Maingi, H. W. Kugel, and A. L. Roquemore, *Rev. Sci. Instrum.* **74**, 5090 (2003).
- ¹³N. Bertelli, E. F. Jaeger, J. C. Hosea, C. K. Phillips, L. Berry, S. P. Gerhardt, D. Green, B. LeBlanc, R. J. Perkins, P. M. Ryan, G. Taylor, E. J. Valeo, and J. R. Wilson, *Nucl. Fusion* **54**, 083004 (2014).
- ¹⁴R. J. Perkins, J. C. Hosea, G. J. Kramer, J.-W. Ahn, R. E. Bell, A. Diallo, S. Gerhardt, T. K. Gray, D. L. Green, E. F. Jaeger, M. A. Jaworski, B. P. LeBlanc, A. McLean, R. Maingi, C. K. Phillips, L. Roquemore, P. M. Ryan, S. Sabbagh, G. Taylor, and J. R. Wilson, *Phys. Rev. Lett.* **109**, 045001 (2012).
- ¹⁵G. J. Kramer, R. V. Budny, A. Bortolon, E. D. Fredrickson, G. Y. Fu, W. W. Heidbrink, R. Nazikian, E. Valeo, and M. A. Van Zeeland, *Plasma Phys. Controlled Fusion* **55**, 025013 (2013).
- ¹⁶J. Kallman, M. A. Jaworski, R. Kaita, H. Kugel, and T. K. Gray, *Rev. Sci. Instrum.* **81**, 10E117 (2010).
- ¹⁷M. A. Jaworski, J. Kallman, R. Kaita, H. Kugel, B. LeBlanc, R. Marsala, and D. N. Ruzic, *Rev. Sci. Instrum.* **81**, 10E130 (2010).
- ¹⁸S. P. Gerhardt, E. Fredrickson, L. Guttadora, R. Kaita, H. Kugel, J. Menard, and H. Takahashi, *Rev. Sci. Instrum.* **82**, 103502 (2011).
- ¹⁹A. Boschi and F. Magistrelli, *Nuovo Cimento* **29**, 487 (1963).
- ²⁰H. S. Butler and G. S. Kino, *Phys. Fluids* **6**, 1346 (1963).
- ²¹S. J. Wukitch, M. L. Garrett, R. Ochoukov, J. L. Terry, A. Hubbard, B. Labombard, C. Lau, Y. Lin, B. Lipschultz, D. Miller, M. L. Reinke, D. Whyte, and Alcator C-Mod Team, *Phys. Plasmas* **20**, 056117 (2013).
- ²²V. I. Bobkov, F. Braun, R. Dux, A. Herrmann, L. Giannone, A. Kallenbach, A. Krivska, H. W. Müller, R. Neu, J.-M. Noterdaeme, T. Pütterich, V. Rohde, J. Schweinzer, A. Sips, I. Zammuto, and ASDEX Upgrade Team, *Nucl. Fusion* **50**, 035004 (2010).
- ²³C. C. Klepper, P. Jacquet, V. Bobkov, L. Colas, T. M. Biewer, D. Borodin, A. Czarnecka, C. Giroud, E. Lerche, V. Martin, M.-L. Mayoral, F. Rimini, G. Sergienko, D. Van Eester, and JET EFDA Contributors, *J. Nucl. Mater.* **438**, S594 (2013).
- ²⁴L. Colas, D. Milanese, E. Faudot, M. Goniche, and A. Loarte, *J. Nucl. Mater.* **390–391**, 959 (2009).
- ²⁵P. Jacquet, F. Marcotte, L. Colas, G. Arnoux, V. Bobkov, Y. Corre, S. Devaux, J.-L. Gardarein, E. Gauthier, M. Graham, E. Lerche, M.-L. Mayoral, I. Monakhov, F. Rimini, A. Sirinelli, D. Van Eester, and JET EFDA Contributors, *J. Nucl. Mater.* **438**, S379 (2013).
- ²⁶J. R. Myra, D. A. D'Ippolito, and M. Bures, *Phys. Plasmas* **1**, 2890 (1994).
- ²⁷C. C. Petty, F. W. Baity, J. S. deGrassie, C. B. Forest, T. C. Luce, T. K. Mau, M. Murakami, R. I. Pinsker, P. A. Politzer, M. Porkolab, and R. Prater, *Nucl. Fusion* **39**, 1421 (1999).
- ²⁸A. Garscadden and K. G. Emeleus, *Proc. Phys. Soc.* **79**, 535 (1962).
- ²⁹J. R. Sanmartin, *Phys. Fluids* **13**, 103 (1970).
- ³⁰P. C. Stangeby, *The Plasma Boundary of Magnetic Fusion Devices, Plasma Physics Series* (Taylor and Francis Group, 2000).
- ³¹M. Abramowitz and I. A. Stegun, *Handbook of Mathematical Functions, National Bureau of Standards Applied Mathematics Series 55* (Courier Corporation, 1964).
- ³²G. F. Matthews, S. J. Fielding, G. M. McCracken, C. S. Pitcher, P. C. Stangeby, and M. Ulrickson, *Plasma Phys. Controlled Fusion* **32**, 1301 (1990).
- ³³T. M. Biewer, R. E. Bell, R. Feder, D. W. Johnson, and R. W. Palladino, *Rev. Sci. Instrum.* **75**, 650 (2004).
- ³⁴T. M. Biewer, R. E. Bell, S. J. Diem, C. K. Phillips, J. R. Wilson, and P. M. Ryan, *Phys. Plasmas* **12**, 056108 (2005).
- ³⁵R. J. Perkins, J.-W. Ahn, R. E. Bell, A. Diallo, S. Gerhardt, T. K. Gray, D. L. Green, E. F. Jaeger, J. C. Hosea, M. A. Jaworski, B. P. LeBlanc, G. J. Kramer, A. McLean, R. Maingi, C. K. Phillips, M. Podesta, L. Roquemore, P. M. Ryan, S. Sabbagh, F. Scotti, G. Taylor, and J. R. Wilson, *Nucl. Fusion* **53**, 083025 (2013).
- ³⁶D. Donovan, R. Nygren, D. Buchenauer, J. Watkins, D. Rudakov, A. Leonard, C. P. C. Wong, and M. Makowski, *Phys. Scr.* **T159**, 014064 (2014).
- ³⁷J. C. Hosea, R. Perkins, M. A. Jaworski, G. J. Kramer, J.-W. Ahn, N. Bertelli, S. Gerhardt, T. K. Gray, B. P. LeBlanc, R. Maingi, C. K. Phillips, L. Roquemore, P. M. Ryan, S. Sabbagh, G. Taylor, K. Tritz, J. R. Wilson, and NSTX Team, *AIP Conf. Proc.* **1580**, 251 (2014).
- ³⁸D. Brunner and B. LaBombard, *Rev. Sci. Instrum.* **83**, 033501 (2012).
- ³⁹R. J. Perkins, J.-W. Ahn, R. E. Bell, N. Bertelli, A. Diallo, S. Gerhardt, T. K. Gray, D. L. Green, E. F. Jaeger, J. C. Hosea, M. A. Jaworski, B. P. LeBlanc, G. J. Kramer, A. McLean, R. Maingi, C. K. Phillips, M. Podesta, L. Roquemore, P. M. Ryan, S. Sabbagh, F. Scotti, G. Taylor, and J. R. Wilson, *AIP Conf. Proc.* **1580**, 81 (2014).
- ⁴⁰D. A. D'Ippolito, J. R. Myra, R. Ochoukov, and D. G. Whyte, *Plasma Phys. Controlled Fusion* **55**, 085001 (2013).